

Supporting Information

Highly Ordered Mesoporous Hydroxide Thin Films through Self-Assembly of Size-Tailored Nano-Building Blocks: A Theoretical-Experimental Approach

Naoki Tarutani[†], Yasuaki Tokudome^{†}, Matías Jobbágy[§], Galo J. A. A. Soler-Illia^{*#}, Qiyun Tang,[‡] Marcus Müller,[‡] Masahide Takahashi[†].*

[†]Department of Materials Science, Graduate School of Engineering, Osaka Prefecture University, Sakai, Osaka 599-8531, Japan

[§] INQUIMAE-CONICET, Facultad Ciencias Exactas y Naturales, Universidad de Buenos Aires, Buenos Aires, C1428EHA, Argentina

[#] Instituto de Nanosistemas, Universidad Nacional de General San Martín, Av. 25 de Mayo y Francia, San Martín, 1650, Argentina.

[‡] Institut für Theoretische Physik, Universität Göttingen, Friedrich-Hund-Platz 1, 37077 Göttingen, Germany

Figure S1	6
Figure S2	7
Figure S3	8
Figure S4	9
Figure S5	10
Figure S6	11
Figure S7	12
Figure S8	13
Figure S9	14
Figure S10	15
Figure S11	16
Table S1	17
References	18

Characterization.

A transmission electron microscope (TEM; JEM-2000FX, JEOL, Japan) and a scanning TEM (STEM; JEM-2100F, JEOL, Japan) were employed at an operating voltage of 200 kV to observe mesostructures of the samples. For the TEM observation, the films after heat-treated at 250 °C were scratched and obtained fine powders were dispersed in ethanol to form a slightly turbid suspension. A small drop of the resultant suspension was placed on a carbon-coated copper mesh grid and dried at room temperature. For the observation of primary particles by STEM, 1 mL of colloidal solutions were diluted with 10 mL of ethanol. 10 μ L of obtained solution was placed on a carbon-coated copper mesh grid and excess solution was removed by swabbing. Powder X-ray diffraction (PXRD) using CuK α radiation (λ = 0.1544 nm) with a diffractometer (Multiflex, Rigaku, Japan) was used to characterize crystal phases of dried powdery samples. Powdery samples were prepared by drying the reacted solution in a glass petri dish at room temperature. The mesoporous characteristics of samples heat treated at 250 °C were analyzed by N₂ sorption measurements (Belsorp-mini II, Bel Japan Inc., Japan). Prior to N₂ sorption measurements, samples were outgassed under vacuum at 200 °C. The specific surface area was estimated by the Brunauer–Emmett–Teller (BET) method, and the pore size distribution was calculated using the Barrett–Joyner–Halenda (BJH) method. Attenuated total reflection Fourier transform infrared (FT-IR) spectroscopy (ALPHA FT-IR spectrometer, Bruker Optik GmbH, Germany) and ultraviolet-visible-near infrared (UV-Vis-NIR) spectroscopy (V-670 spectrophotometer, JASCO Corp.) were used to analyze chemical bonding and coordination state of Ni(II). In-situ FT-IR spectra were recorded from 5000–375 cm⁻¹ at 4 cm⁻¹ resolutions every 1 min using a home-made close-sealed polydimethylsiloxane cell. In-situ UV-Vis-NIR spectra were recorded from 250–1350 nm at 1 nm resolutions with a scan speed of 2000 nm/min every 1 min using a 1 cm width close-sealed silica cell. In-situ data of conductivity and pH of solutions were collected every 5 s after reaction start using a water quality meter (D74, Horiba, Japan) with respective glass electrodes (3552-10D and 9618-10D). The relative Ni²⁺ amount was estimated from the calibration curve, $\log(\sigma) = 0.777 \times \log(C_{Ni}) + 3.69$, where σ and C_{Ni} are the conductivity of the solution and the concentration of Ni²⁺, respectively. The calibration curve was obtained with an ethanol solvent at different C_{Ni} values (0.001, 0.01, 0.1, 1 mol/L). The conductivities of ethanol (1.14 μ S/cm) and acrylic acid (1.76 μ S/cm at 1.0 mol/L in ethanol) are small enough compared to that of NiCl₂·6H₂O (3.49×10³ μ S/cm at 0.5 mol/L in ethanol), confirming that the change of σ is proportionally correlated to the change of C_{Ni} in the measured concentration range. Thermogravimetric–differential thermal analysis (TG–DTA; Thermo Plus Evo, Rigaku, Japan) was carried out to estimate an amount of organic compound contents at a ramp rate of 10 °C/min while continuously supplying air.

Calculation of NBB diameter using X-ray scattering measurement.

The small angle X-ray scattering (SAXS) measurement was performed to characterize formed particle size and mesostructures with the beamline of the Brazilian Synchrotron Light Laboratory (LNLS, Brazil D11A-SAXS1-18927 and 20160366). X-ray with a wavelength, λ , of 0.1544 nm was used. A linear position sensitive X-ray detector and a multi-channel analyzer were used to collect the SAXS signal. For the characterization of cast solid samples, polyimide tape was employed to pack an enough amount of powder, and normal transmission was used (90 °). For in-situ analysis of liquid samples, SAXS patterns were collected every 1 min (45 s for accumulation time and 15 s for dead time). The first pattern was collected reaction time from 1.5 to 2.5 min, which is denoted as pattern of 2 min reacted solution. A sample-to-detector

distance was set at 904.6242 mm, corresponding to a scattering vector range of 0.1–4.8 nm⁻¹. After the removal of background, the scattering profiles were circularly averaged and plotted against the scattering vector, q , according to the following equation;

$$q = \frac{\pi}{\lambda} \sin 2\theta$$

where θ is scattering angle. To evaluate particle size from experimental SAXS patterns, we employed a unified equation proposed by Beaucage and Schaefer,^{R1,R2} which was developed to describe scattering from objects with hierarchical structures. The unified equation for the hierarchical structure with multiple structural levels is described as follows;

$$I(q) \approx \sum_{i=1}^n (G_i \exp\left(\frac{-q^2 R_{gi}^2}{3}\right) + B_i \exp\left(\frac{-q^2 R_{g(i+1)}^2}{3}\right) \times \left\{ \left[\operatorname{erf}\left(\frac{q R_{gi}}{\sqrt{6}}\right) \right]^{P_i} \right\})$$

where n is the number of structure levels, R_{gi} is the gyration radius of the i th level, P_i is the power-law exponent, G_i is the Guinier prefactor, and B_i is the prefactor specific to the type of power-law scattering falls. The particle diameter of i th level, D_i , is calculated by using spherical particle model as follows;

$$R_{gi} = \frac{D_i}{2} \sqrt{\frac{3}{5}}$$

Typical results of the fitting on the sample prepared without carboxylic acid (denoted as AA0-30) are shown in Fig S1. The sample shows a nanostructure of aggregated nanoparticles (**TEM image Figure S1a**). This hierarchical structure was fitted by the unified equation $n = 1$ and 2, respectively (**Figure S1b and c**). The fitting with $n = 2$ led to more accurate results, confirming the hierarchical aggregated structure of the samples observed by TEM image. On the other hand, the SAXS curves measured on the sample of AA2.0-*tt* can be well fitted with $n = 1$, suggesting the material possess a single-level-structure, *i.e.*, nanoparticles without aggregation.

Simulation study.

We consider n amphiphilic surfactants and n_p nanoparticles in a volume V with periodic boundary conditions at a constant temperature, T . The PEO-based surfactant, F127, is represented by a bead-spring model with soft, non-bonded interactions.^{R3} This top-down model incorporates bonded interactions that describe the linear molecular architecture of the amphiphiles and non-bonded interactions that give rise to microphase separation in the surfactant solution.

We discretize the molecular backbone of the amphiphilic surfactants into N beads with the neighboring beads connected by harmonic springs

$$\frac{\mathcal{H}_b[\{\mathbf{r}_{i,s}\}]}{k_B T} = \sum_{i=1}^n \sum_{s=1}^{N-1} \frac{3(N-1)}{2R_{e0}^2} [\mathbf{r}_{i,s+1} - \mathbf{r}_{i,s}]^2$$

here $\mathbf{r}_{i,s}$ with $i = 1, \dots, n$ and $s = 1, \dots, N$ represents the coordinate of the s^{th} bead on surfactant i . $R_{e0} \approx \sqrt{6}R_g = \sqrt{6} \times 3.46 \text{ nm} = 8.475 \text{ nm}$ is the end-to-end distance of the unperturbed chain molecules. We take this value from SAXS experiments, neglecting the influence of the screened excluded volume effects.

The surfactant, F127, is comprised of 70 hydrophobic PPO repeat units $-\text{[CH}_2\text{CH(CH}_3\text{)O]}-$ and two blocks of hydrophilic PEO repeating units $-\text{[CH}_2\text{CH}_2\text{O]}-$, each block of 106 repeat units. Thus the F127 has a BAB-like triblock copolymer structure, with B corresponding to the PEO block.^{R4} Ignoring the volume difference of the two bead species, the hydrophobic volume fraction of the surfactant can be roughly estimated as, $f_A = 70/(70+212) \approx 0.25$. In our model, we

discretize the chain contour into $N = 40$ coarse-grained beads with a structure of $B_{14}A_{12}B_{14}$, similar as F127 but with a little larger f_A of 0.3.

The mass density of F127 is 1.095 g/cm^3 with the molecular weight of 13800 g/mol . Thus the number density of F127 is $\rho_0/N \simeq 79.348 \text{ mol/m}^3$. These values result in a square root of the invariant degree of polymerization, $\sqrt{N} = \rho_0 R_{e0}^3/N \simeq 29$, i.e., the number of amphiphiles is given by $n = \sqrt{N}V/R_{e0}$. This invariant degree of polymerization gives a very low polymer density in our model, which generates large composition fluctuations. Therefore, we choose $\sqrt{N} = 128$ in the following simulations.

Here we model the nano building blocks as spherical NPs. As the size of nano-building blocks changes in experiments, we choose the NP-NP interact via a Hamaker potential^{R5}:

$$\frac{U_{PP}(r, R)}{k_B T} = f(x) = \begin{cases} \infty, & d < 2R_{core} \\ -\varepsilon_{PP} \left[\frac{2R^2}{(r + 2R)^2 - 4R^2} + \frac{2R^2}{(r + 2R)^2} + \ln \frac{(r + 2R)^2 - 4R^2}{(r + 2R)^2} \right], & d > 2R_{core} \end{cases}$$

here r denotes the distance between the particle centers, and R is the NP radius. $R_{core} = R - \xi$ and $\xi = 0.1R_{e0}$ denote the core radius of the NP and the width of its surface, respectively. The diameter of the spherical NPs is changed from 2.54 nm to 6.78 nm , in analogy to experimental measurements. Here the cut off of the Hamaker potential is chosen as $r_{cut} = 4R_{core}$, and the potential is shift to 0 at $r = r_{cut}$.

To capture the non-bonded interactions between surfactants and NPs, we employ an excess free-energy functional of the local normalized densities of the different species, $\phi_A(\mathbf{r})$, $\phi_B(\mathbf{r})$, and $\phi_P(\mathbf{r})$. The local A density $\phi_A(\mathbf{r})$ is defined as:

$$\phi_A(\mathbf{r}|\{\mathbf{r}_{i,s}\}) = \frac{1}{\rho_0} \sum_{i=1}^n \sum_{s=1}^N \gamma_{i,s} \delta(\mathbf{r} - \mathbf{r}_{i,s})$$

here $\gamma_{i,s} = 1$ if the s^{th} segment is of type A and 0 for B . The microscopic B density takes a similar formula. In our simulation, we model the nickel-oxo subunits as spherical nanoparticles, with the density defined as $\phi_P(\mathbf{r}) = \sum_{i=1}^{n_p} \theta(|\mathbf{r} - \mathbf{r}_i|)$. Here

$$\theta(d) = \begin{cases} 1, & d < R_{core} \\ \frac{1}{2} \left(1 + \cos \left[\frac{(d - R_{core})\pi}{\xi} \right] \right), & R_{core} \leq d \leq R \\ 0, & d > R \end{cases}$$

describes the shape of the nanoparticle. It is worthy to note that the NP width defined above accounts for the irregular shape of the nickel-oxo subunits^{R6}, thus this width does not relate to its local environment.

Based on these densities, the density fluctuations of the liquid mixture of amphiphiles and NPs can be considered by:

$$\frac{\mathcal{H}_{nb}^{comp}}{k_B T} = \sqrt{N} \int \frac{d\mathbf{r}}{R_{e0}^3} \frac{\kappa N}{2} [\phi_A(\mathbf{r}) + \phi_B(\mathbf{r}) + \phi_P(\mathbf{r}) - 1]^2$$

Here we choose $\kappa N = 150$, which physically implies a near-incompressibility of the liquid.

The repulsion between the hydrophobic and hydrophilic beads of the surfactant is accounted for by the term

$$\frac{\mathcal{H}_{nb}^{AB}}{k_B T} = -\sqrt{N} \int \frac{d\mathbf{r}}{R_{e0}^3} \frac{\chi N}{4} [\phi_A(\mathbf{r}) - \phi_B(\mathbf{r})]^2$$

In the Hamiltonian, we choose the Flory-Huggins parameter $\chi N = 60$ between the two blocks of the amphiphiles in our simulation which is strong enough to introduce microphase separation of F127.

The interaction between the NPs and surfactants is modeled by:

$$\frac{\mathcal{H}_{\text{nb}}^{\text{AB-P}}}{k_{\text{B}}T} = \sqrt{\mathcal{N}} \int \frac{d\mathbf{r}}{R_{\text{e0}}^3} \left\{ -\frac{\delta N_{\text{AP}}}{4} [\varphi_{\text{A}}(\mathbf{r}) - \varphi_{\text{P}}(\mathbf{r})]^2 + \frac{\delta N_{\text{BP}}}{4} [\varphi_{\text{B}}(\mathbf{r}) - \varphi_{\text{P}}(\mathbf{r})]^2 \right\}$$

here $\delta N_{\text{BP}} = 120$ captures the magnitude of the affinity between the titanium clusters and PEO,^{R4,R7} while $\delta N_{\text{AP}} = 100$ represents the repulsion between NPs and the hydrophobic PPO blocks.

We compute all these densities on a collocation grid, see details in reference.^{R4} The simulation parameters are listed in table below;

Parameter	Value	Parameter	Value
$\chi_{\text{AB}}^{\text{N}}$	60	$\sqrt{\mathcal{N}}(\text{F127})$	128
δN_{AP}	100	N	40 = 14 + 12 + 14
δN_{BP}	120	f_{A}	0.3
κ^{N}	150	δR	0.01 R_{e0}
ε_{PP}	1.0	R	0.15, 0.20, ..., 0.40 R_{e0}
n_{P}	Change with R	R_{core}	$R - 0.10R_{\text{e0}}$
System size	$7.2 \times 7.2 \times 0.9R_{\text{e0}}^3$	Grid	$216 \times 216 \times 27$

For all the simulations, the initial states are randomly distributed NPs and polymers. The simulations are run for enough long time to ensure the NP configurations are stable, i.e., the dispersity index DI measured from 10 independent runs does not change as the simulation time increases, see Fig. S6f. Figure S5a-e show the typical snapshots of mesostructures formed with NBBs and F127 at different D_{NBB} .

Preparation of referential α -Ni(OH)₂ intercalated with acrylate anions.

NiCl₂·6H₂O (1.25 mmol) and acrylic acid (2.50 mmol) were dissolved in an ethanol (2.5 mL). Ethanolic solution of sodium hydroxide (2.0 mol/L, 2.5 mL) was added to the clear precursor solution and stirred for 24 h at room temperature (20–25 °C). Obtained precipitates were washed with water by suction filtration and dried at 60 °C.

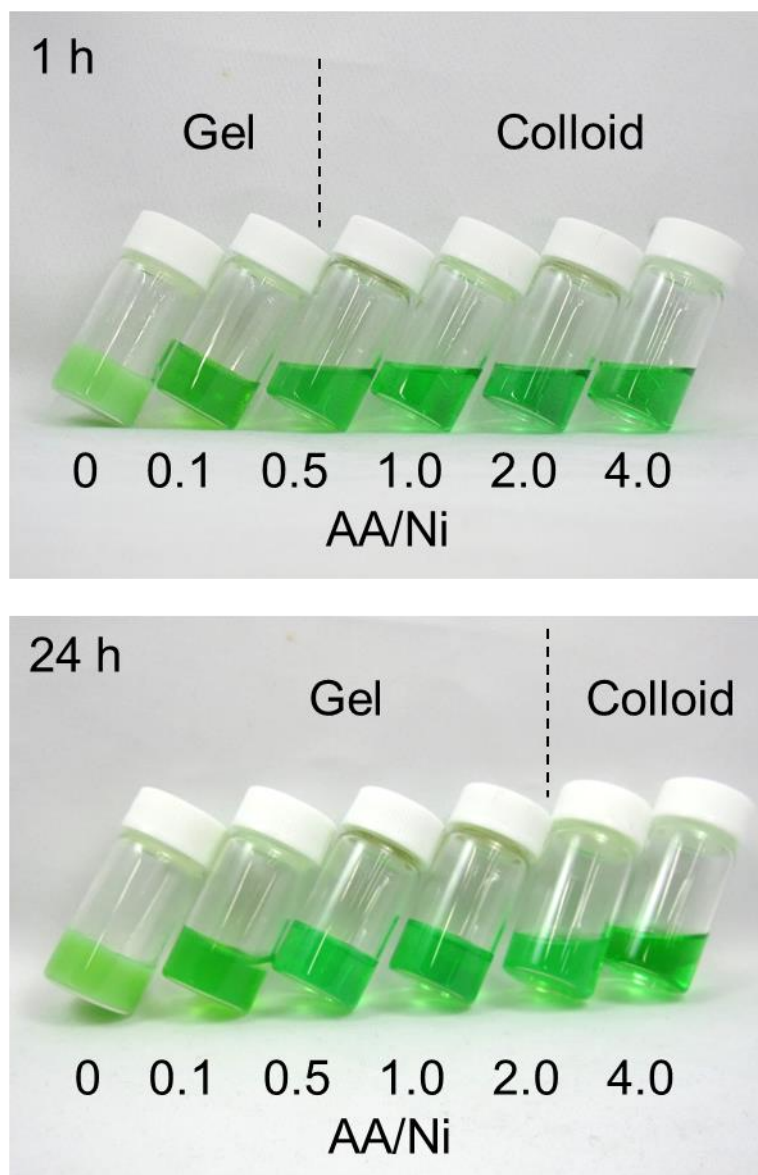


Figure S1. Photo image of samples after 1 h and 24 h reaction. Upon an increase in the amount of acrylic acid, the resultant products changed from opaque gel (left side) to transparent colloidal solutions (right side). The compositions of sample solutions are as follows: $\text{NiCl}_2 \cdot 6\text{H}_2\text{O}$ (1.25 mmol), acrylic acid (0–5.0 mmol), ethanol (2.5 mL), and propylene oxide (7.5 mmol). The reaction time was measured since the addition of propylene oxide.

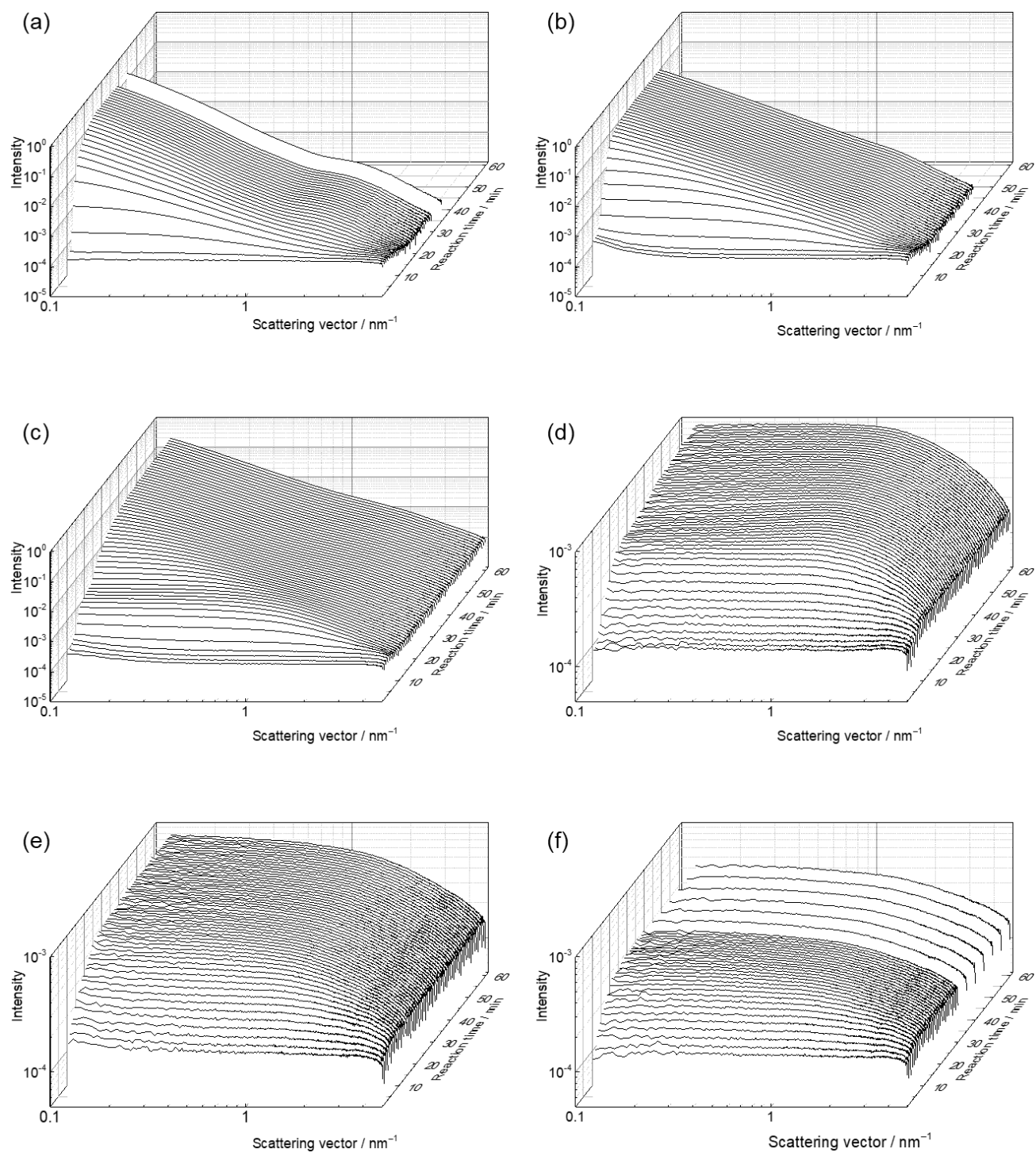


Figure S2. Time-dependent change of SAXS patterns of (a) AA-0- t , (b) AA-0.1- t , (c) AA-0.5- t , (d) AA-1.0- t , (e) AA-2.0- t , (f) AA-4.0- t ($t = 1-60$).

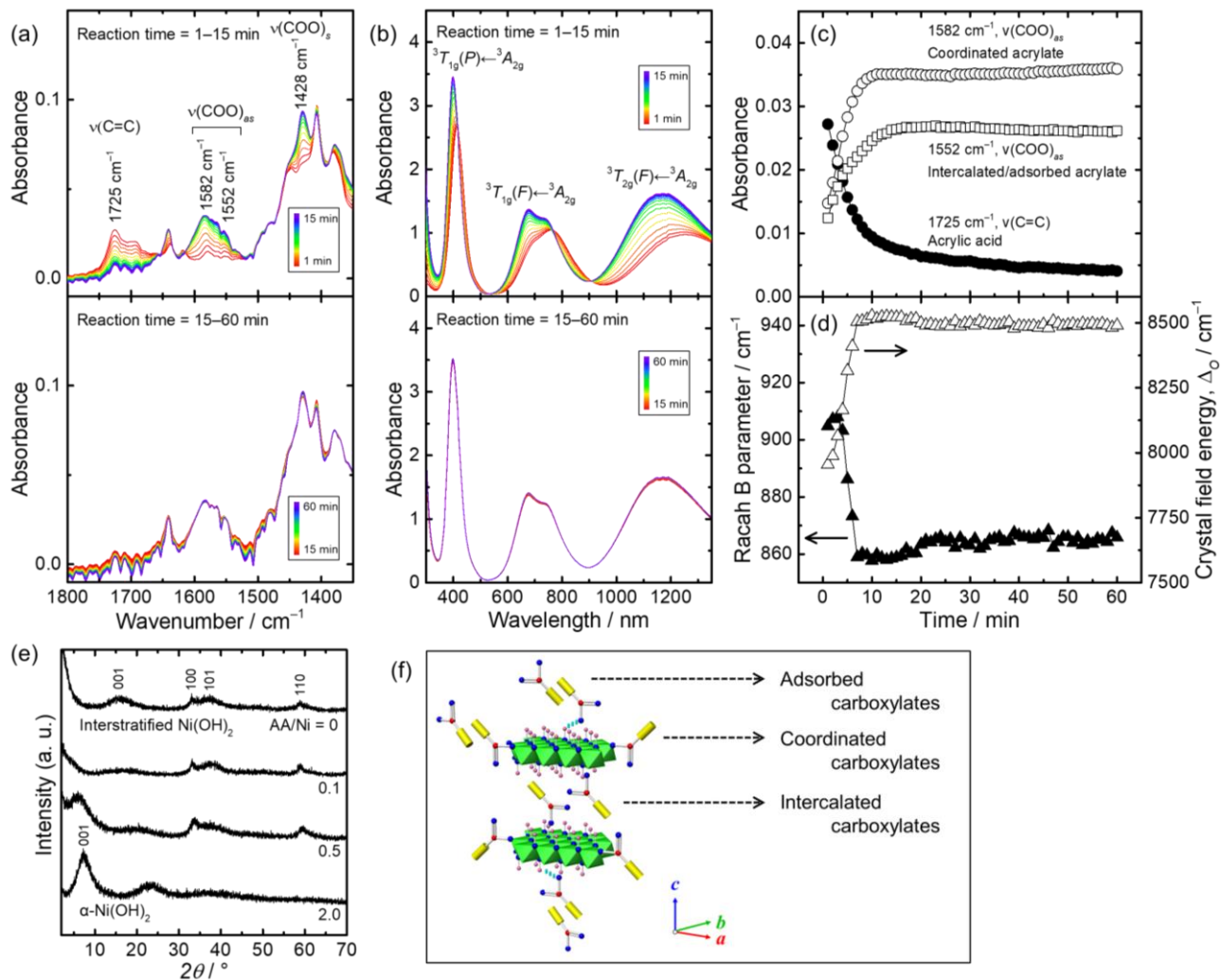


Figure S3. In-situ (a) FT-IR and (b) UV-Vis-NIR spectra of AA-2.0- t ($t = 1-60$). The peaks in FT-IR spectra of 1725, 1582–1552, and 1428 cm^{-1} are vibrations of $\nu(\text{C}=\text{C})$ (acrylic acid), asymmetric $\nu(\text{COO})_{as}$ (acrylate) and symmetric $\nu(\text{COO})_s$ (acrylate), respectively. The frequency differences, $\Delta = \nu(\text{COO})_{as} - \nu(\text{COO})_s$, were 124–154 cm^{-1} , which is relatively higher or comparable to that of free acrylate ($\Delta = 110-140 \text{ cm}^{-1}$).^{R8,R9} These results suggest acrylate ions are unidentately coordinated to Ni(II) and intercalated/adsorbed on $\alpha\text{-Ni}(\text{OH})_2$ sheets.^{R10} The peaks in UV-Vis-NIR spectra centered at around 1250, 760, and 410 nm are assigned as transitions of ${}^3A_{2g} \rightarrow {}^3T_{2g}(\text{F})$, ${}^3A_{2g} \rightarrow {}^3T_{1g}(\text{F})$, and ${}^3A_{2g} \rightarrow {}^3T_{1g}(\text{P})$, respectively, which is a typical feature of octahedral coordination state of Ni complex.^{R11-R13} Racah B parameter and crystal field energy of NBB reached constant values in 10 min reaction to give 902 cm^{-1} and 8520 cm^{-1} , respectively. The values are comparable with reported $\alpha\text{-Ni}(\text{OH})_2$ (820–925 cm^{-1} and 8600–8800 cm^{-1}),^{R9,R13} which indicates the local structure of Ni(II) is same as brucite-like structure. (c)(d) Significant changes in FT-IR (peak intensities) and UV-Vis-NIR (Racah B parameter and crystal field energy) were observed within 20–30 min, which is a good agreement with the results in Figure 2a. (e) PXRD patterns of dried powders, prepared with molar ratio of AA/Ni = 0–2.0 after 24 h reaction. The crystal structure of samples prepared from AA/Ni = 0–0.1 and 0.5–2.0 solutions are assigned as interstratified $\text{Ni}(\text{OH})_2$ and $\alpha\text{-Ni}(\text{OH})_2$, respectively.^{R14} (f) Schematic illustration of obtained $\alpha\text{-Ni}(\text{OH})_2$ NBBs (atoms are partially hidden for easy understanding) (the symbols: green octahedral is Ni, blue sphere is O, red sphere is C, pink sphere is H, yellow rod is organic group, and light blue dot line is hydrogen bonding).

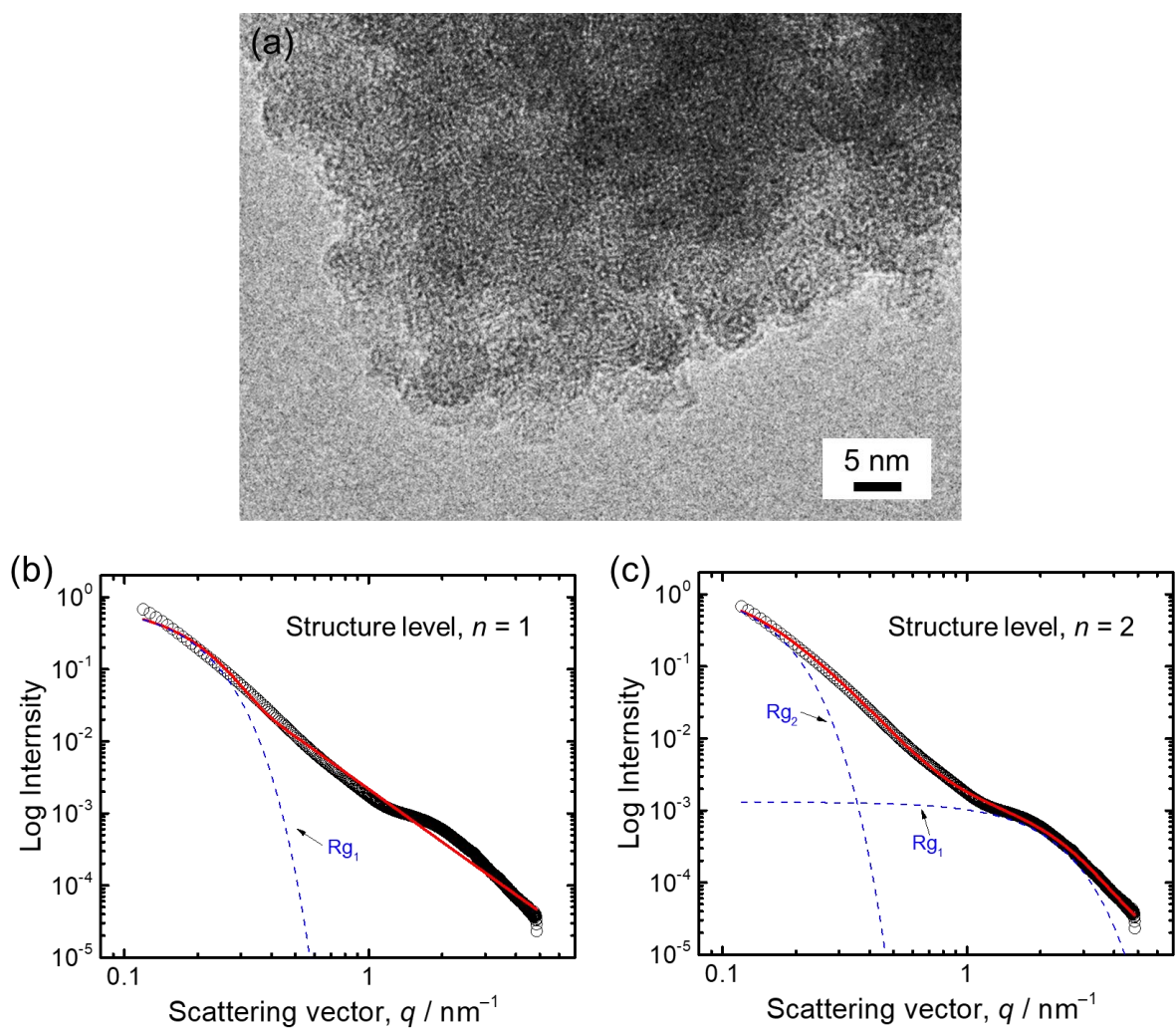


Figure S4. (a) TEM image of AA-0-30 dried on a TEM copper grid. (b) and (c) SAXS pattern of AA-0-30 (open circle) with fitting curves (red solid line) using unified equation. The structure level of $n = 1$ and $n = 2$ were employed in (b) and (c), respectively. Blue dot line shows contribution of first and second level structures on fitted patterns.

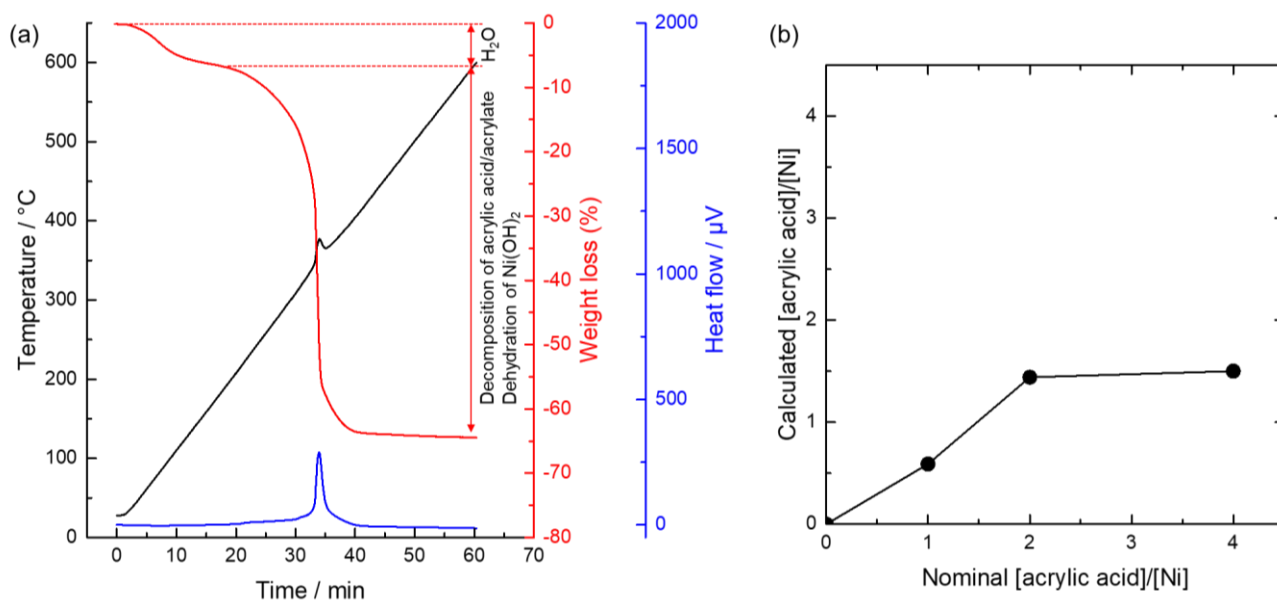


Figure S5. (a) TG-DTA curves of AA-2.0-60. The weight loss up to 200 °C was eliminated from calculation because it comes from removal of adsorbed water. The sharp exothermic peak around 350 °C with weight loss implies the decomposition of acrylic acid/acrylate and dehydration of layered nickel hydroxide. It was reported that carboxylate intercalate layered nickel hydroxides shows similar strong exothermic event which may be due to catalytic oxidation of the organic species.^{R10,R15,R16} In our case, the strong exothermic peak may hinder endothermic peak due to dehydration of layered nickel hydroxide. Incorporated amount of acrylic acid/acrylate was calculated from TG-DTA curves on the premise that final products were NiO. (b) The [acrylic acid]/[Ni] of NBBs as a function of nominal [acrylic acid]/[Ni]. The weight loss due to dehydration of Ni(OH)₂ and decomposition of acrylic acid/acrylate were 44.8, 61.7, 62.7 % in case of AA-1.0, AA-2.0 and AA-4.0, respectively.

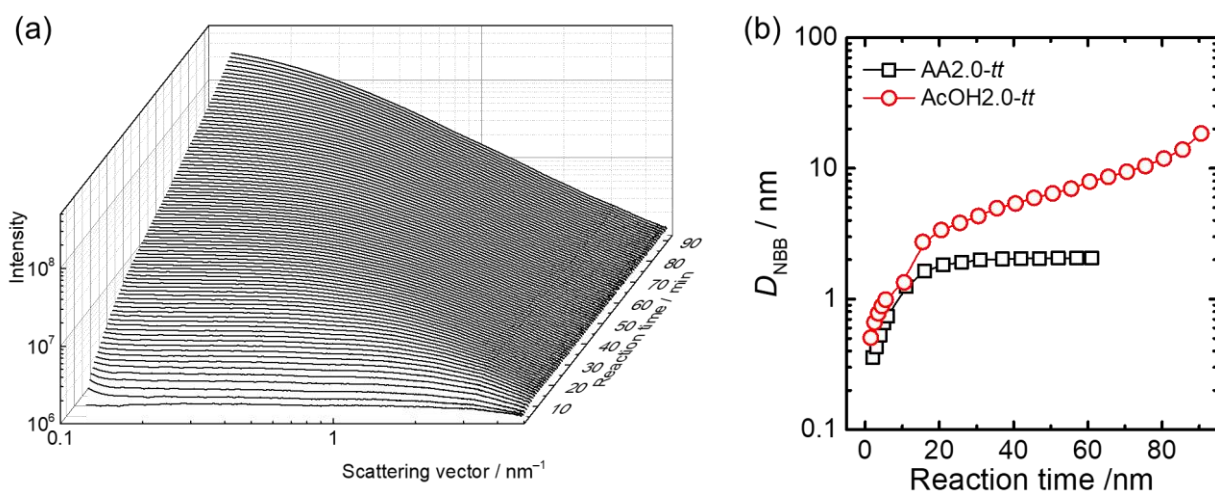


Figure S6. Time-dependent change of (a) SAXS pattern of AcOH-2.0-F- t ($t = 1-90$) and (b) D_{NBB} prepared from AA/Ni = 2.0 solutions of AA-2.0- t ($t = 1-60$) (black) and AcOH-2.0-F- t ($t = 1-60$) (red). The growth kinetics of D_{NBB} were comparable, regardless of the addition of F127.

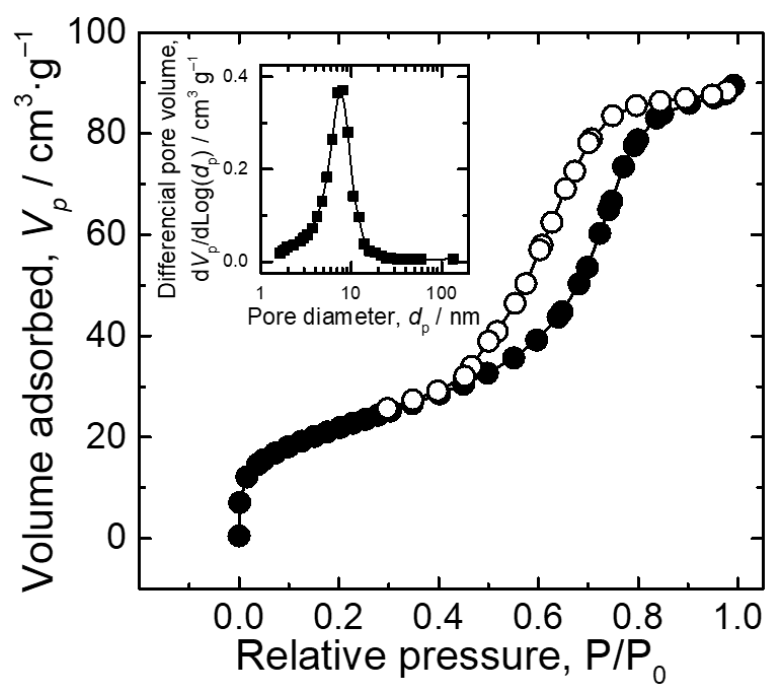


Figure S7. N₂ adsorption/desorption (close/open circle) isotherms of films prepared from AA-2.0-F-5 after heat treatment at 120 °C for 2 h and 250 °C for 2 h. The N₂ adsorption/desorption isotherm is classified into a type IV shape with a hysteresis loop of H1. Pore diameter, wall thickness, specific surface area, and pore volume are 7.6 nm, 6.5 nm, 79.2 m²/g, and 0.140 cm³/g, respectively.

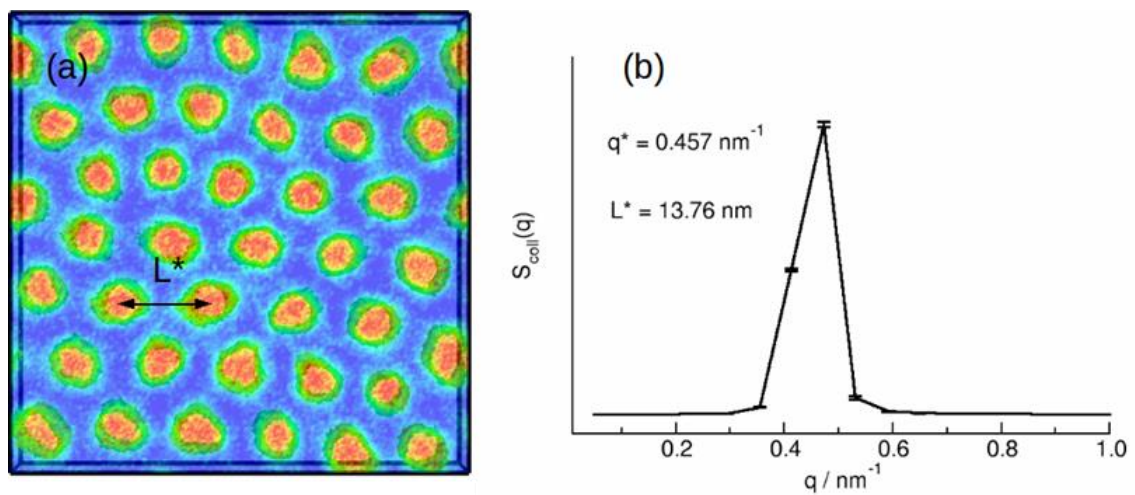


Figure S8. (a) Snapshots of F127 molecules without NBBs. The Flory-Huggins parameters between PPO and PEO were chosen as 100, and other parameters are the same as in the Table. The system size is $61.02 \times 61.02 \times 7.63 \text{ nm}^3$. The red spheres and blue regions represent the hydrophobic cores and PEO domains. (b) Collective structure factor calculated and averaged from 50 snapshots.

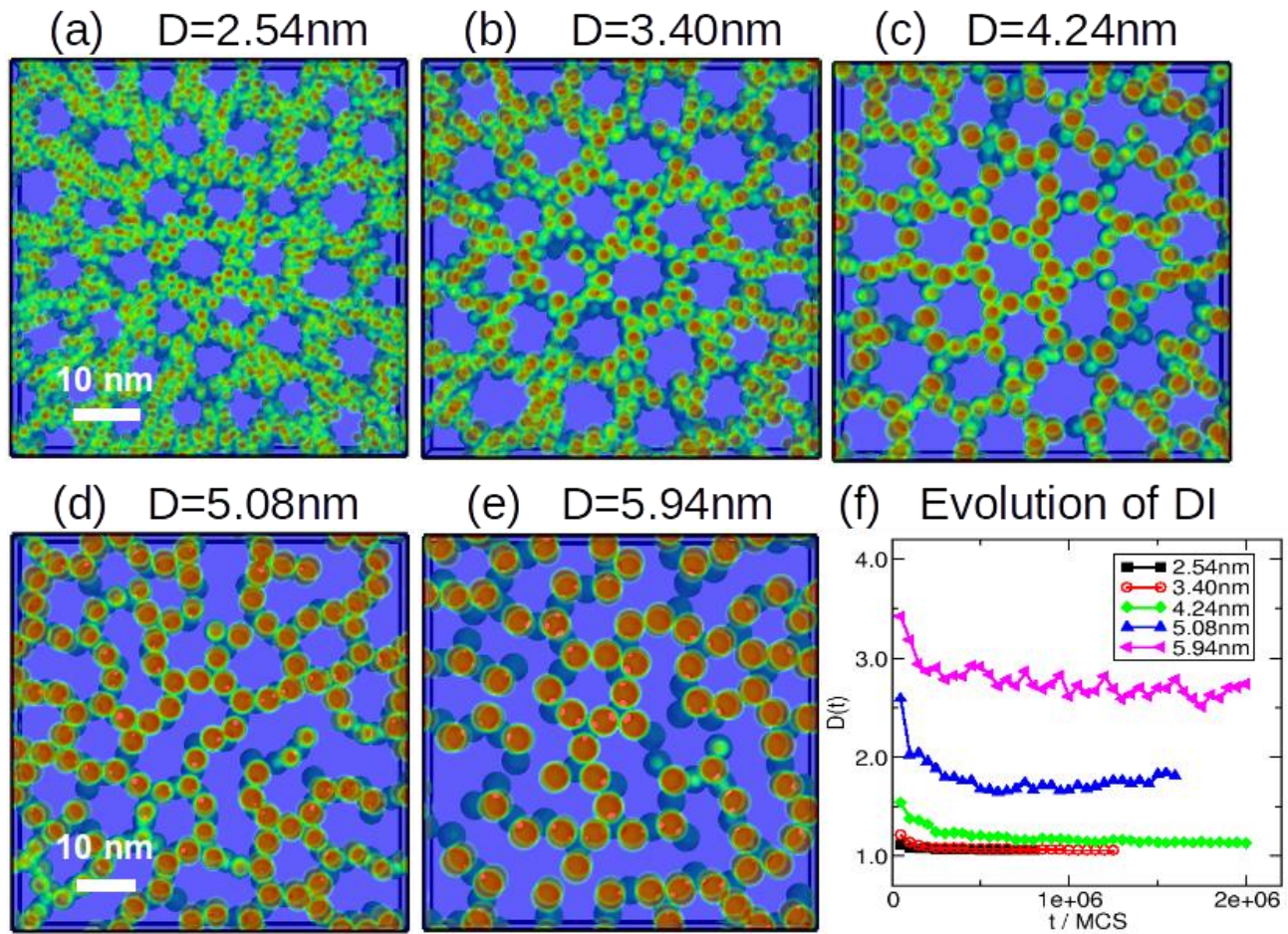


Figure S9. Typical snapshots of mesostructures formed with NBBs and F127 with $D_{\text{NBB}} =$ (a) 2.54 nm at $t = 846000$ MCS (Monte-Carlo steps), (b) 3.40 nm at $t = 1301000$ MCS, (c) 4.24 nm at $t = 2039000$ MCS, (d) 5.08 nm at $t = 1650000$ MCS, and (e) 5.94 nm at $t = 2115000$ MCS. The system size of (a)–(c) is $61.02 \times 61.02 \times 7.63 \text{ nm}^3$ and of (d)–(e) is $68.65 \times 68.65 \times 7.63 \text{ nm}^3$. The red spheres, green rings and blue regions are the NBB core, the interface and the F127 filled parts, respectively. (f) Time evolution of dispersity index at different diameters of NBBs.

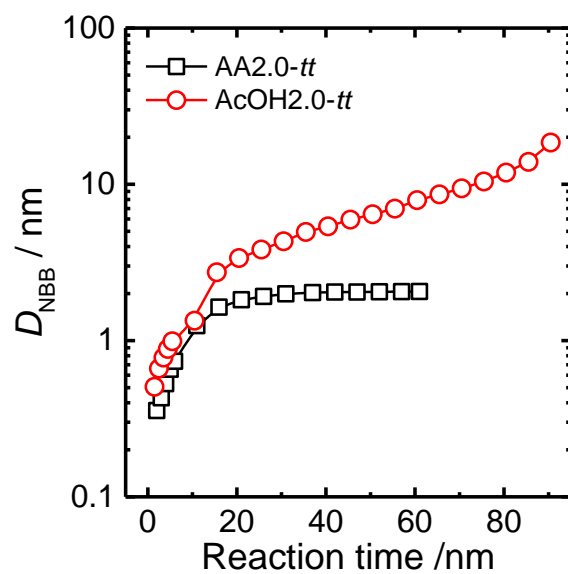


Figure S10. Time-dependent growth of NBB prepared from acrylic acid (black square, AA-2.0- t ($t = 1$ –60 min)) and acetic acid (red circle, AcOH-2.0- t ($t = 1$ –90 min)) incorporated precursor solutions.

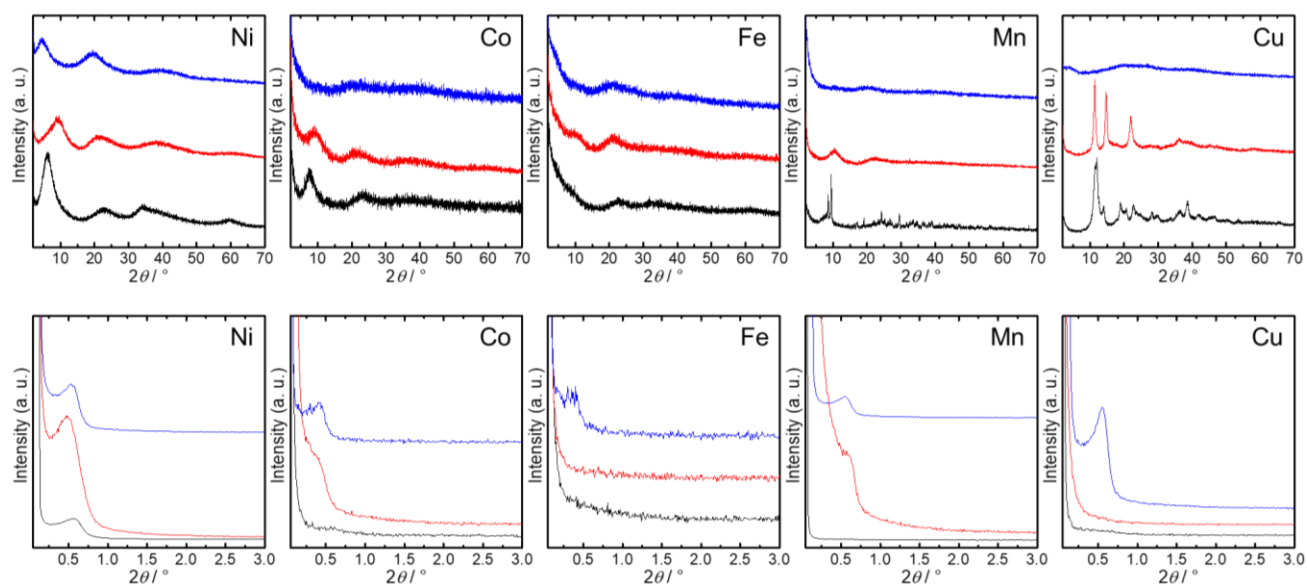
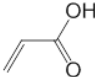
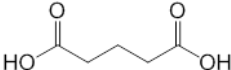
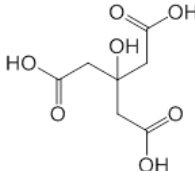


Figure S11. (upper line) PXRD patterns of dried powders and (lower line) SAXS patterns of cast films. Black, red, and blue lines are samples prepared with acrylic acid, glutaric acid, and citric acid, respectively. The molar ratio, reaction time, crystallite size and meso-periodicity of each samples are summarized in Table S1.

Table S1. Crystallite size and mesoperiodicity of samples prepared from the precursor solution including specific metal ion and carboxylic acid.

		Weak → Strong		
				
		Acrylic acid	Glutaric acid	Citric acid
<div>Slow</div> <div>Crystallization</div> <div>Rapid</div>	Metal ion (Order of k_{aq}^a / s^{-1})	ID: Ni-AA-4.0-90 $D_{\text{cry}}^b = 2.00 \text{ nm}$ $D_{\text{meso}}^c = 15.1 \text{ nm}$	Ni-Glu-1.0-2 1.17 nm 16.1 nm	Ni-Cit-0.67-0.5 1.74 nm 18.4 nm
	Ni^{2+} (10^4)			
	Co^{2+} (10^5)	Co-AA-4.0-90 2.35 nm 15.1 nm	Co-Glu-1.0-5 1.19 nm 19.8 nm	Co-Cit-0.67-0.5 1.86 nm 20.7 nm
	Fe^{2+} (10^6)	Fe-AA-4.0-90 N/A N/A	Fe-Glu-1.0-2 1.15 nm N/A	Fe-Cit-0.67-0.5 1.87 nm 22.5 nm
	Mn^{2+} (10^6)	Mn-AA-4.0-360 51 nm N/A	Mn-Glu-1.0-5 1.81 nm 14.3 nm	Mn-Cit-0.67-0.5 0.62 nm 16.0 nm
	Cu^{2+} (10^8)	Cu-AA-4.0-90 21 nm N/A	Cu-Glu-1.0-5 19 nm N/A	Cu-Cit-0.67-0.5 1.38 nm 16.0 nm

^a Rate constant of H_2O substitution in the inner coordination sphere of metal ions.³⁹ ^b Crystallite size calculated from the strongest peak in corresponding PXRD patterns of dried powders using Scherrer's equation. ^c Mesoperiodicity calculated from corresponding SAXS patterns of casted-film after dried at room temperature for 2 h.

References in supporting information

- (R1) Beaucage, G.; Schaefer, D.W. Structural studies of complex systems using small-angle scattering: a unified Guinier/power-law approach. *J. Non-Cryst. Solids* **1994**, *172-174*, 797–805.
- (R2) Beaucage, G. Approximations Leading to a Unified Exponential/Power-Law Approach to Small-Angle Scattering. *J. Appl. Cryst.* **1995**, *28*, 717–728.
- (R3) Müller, M. Studying Amphiphilic Self-assembly with Soft Coarse-Grained Models. *J. Stat. Phys.* **2011**, *145*, 967–1016.
- (R4) Tang, Q.; Angelomé, P. C.; Soler-Illia, G. J. A. A.; Müller, M. Formation of ordered mesostructured TiO₂ thin films: a soft coarse-grained simulation study. *Phys. Chem. Chem. Phys.* **2017**, *19*, 28249–28262.
- (R5) Hamaker, H. C. The London—van der Waals attraction between spherical particles. *Physica* **1937**, *4*, 1058–1072.
- (R6) Kallala, M.; Sanchez, C.; Cabane, B. “Structures of inorganic polymers in sol-gel processes based on titanium oxide. *Phys. Rev. E* **1993**, *48*, 3692–3704.
- (R7) Soler-Illia, G. J. A. A.; Sanchez, C. Interactions between poly(ethylene oxide)-based surfactants and transition metal alkoxides: their role in the templated construction of mesostructured hybrid organic–inorganic composites. *New. J. Chem.* **2000**, *24*, 493–499.
- (R8) Fairheller, W. R.; Katon, J. E. The vibrational spectra of acrylic acid and sodium acrylate. *Spectrochim. Acta* **1967**, *23*, 2225–2232.
- (R9) Deacon, G.B.; Phillips R.J. Relationships between the carbon-oxygen stretching frequencies of carboxylato complexes and the type of carboxylate. *Coord. Chem. Rev.* **1980**, *33*, 227–250.
- (R10) Poul, L.; Jouini, N.; Fiévet, F. Layered Hydroxide Metal Acetates (Metal = Zinc, Cobalt, and Nickel): Elaboration via Hydrolysis in Polyol Medium and Comparative Study. *Chem. Mater.* **2000**, *12*, 3123–3132.
- (R11) Tanabe, Y.; Sugano, S. On the Absorption Spectra of Complex Ions. I. *J. Phys. Soc. Jpn.* **1954**, *9*, 753–766.
- (R12) Tanabe, Y.; Sugano, S. On the Absorption Spectra of Complex Ions II. *J. Phys. Soc. Jpn.* **1954**, *9*, 766–779.
- (R13) Manceau, A.; Calas, G.; Decarreau, A. Nickel-Bearing Clay Minerals: I. Optical Spectroscopic Study of Nickel Crystal Chemistry. *Clay Miner.* **1985**, *20*, 367–387.
- (R14) Rajamathi, M.; Subbanna, G. N.; Kam, P. V. On the existence of a nickel hydroxide phase which is neither α nor β . *J. Mater. Chem.* **1997**, *7*, 2293–2296.
- (R15) Taibi, M.; Ammar, S.; Jouini, N.; Fiévet, F.; Molinié, P.; Drillon, M. Layered nickel hydroxide salts: synthesis, characterization and magnetic behaviour in relation to the basal spacing. *J. Mater. Chem.* **2002**, *12*, 3238–3244.
- (R16) Rojas, R.; Barriga, C.; Ulibarri, M. A.; Malet, P.; Rives, V. Layered Ni(II)-Zn(II) hydroxyacetates. Anion exchange and thermal decomposition of the hydroxysalts obtained. *J. Mater. Chem.* **2002**, *12*, 1071–1078.